










# Magneto-Thermal Thin Shell Approximation for 3D Finite Element Analysis of No-Insulation Coils

Erik Schnaubelt , Sina Atalay , Mariusz Wozniak , Julien Dular , Christophe Geuzaine , Benoît Vanderheyden , Nicolas Marsic , Arjan Verweij , and Sebastian Schöps , *Member, IEEE*

**Abstract**—For finite element (FE) analysis of no-insulation (NI) high-temperature superconducting (HTS) pancake coils, the high aspect ratio of the turn-to-turn contact layer (T2TCL) leads to meshing difficulties which result in either poor quality mesh elements resulting in a decrease of the solution accuracy or a high number of degrees of freedom. We proposed to mitigate this issue by collapsing the T2TCL volume into a surface and using a so-called thin shell approximation (TSA). Previously, two TSA have been introduced, one to solve the heat equation and the other for an  $\vec{H} - \phi$  magnetodynamic formulation. In this work, we propose to combine the magnetodynamic and thermal TSA to create a coupled magneto-thermal TSA for three-dimensional FE analysis. Particular attention is paid to the detailed derivation of the coupling terms. In the context of NI HTS pancake coils, the TSA represents the electric and thermal contact resistance of the T2TCL. For the HTS coated conductor (CC) itself, an anisotropic homogenization is used which represents its multi-layered structure. In axial and azimuthal direction, it resolves the current sharing between the HTS and other layers of the CC. The coupled TSA formulation is verified against a reference model with volumetric T2TCL. The coupled TSA is shown to significantly reduce the solution time as well as the manual effort required for high-quality meshes of the T2TCL. The implementation is open-source and a reference implementation is made publicly available.

**Index Terms**—Finite elements,  $\vec{H} - \phi$  formulation, magneto-thermal analysis, no-insulation coil, thin shell approximation.

## I. INTRODUCTION

NO-INSULATION (NI) pancake coils [1] have no turn-to-turn electrical insulation and are popular due to their high

Manuscript received 26 September 2023; revised 23 November 2023; accepted 4 December 2023. Date of publication 8 December 2023; date of current version 26 December 2023. The work of Erik Schnaubelt was supported in part by the Wolfgang Gentner Programme of the German Federal Ministry of Education and Research under Grant 13E18CHA and in part by the Graduate School Computational Engineering within the Centre for Computational Engineering at the Technical University of Darmstadt. (*Corresponding author: Erik Schnaubelt.*)

Erik Schnaubelt is with CERN, 1211 Meyrin, Switzerland, and also with the Technical University of Darmstadt, 64289 Darmstadt, Germany (e-mail: erik.schnaubelt@cern.ch).

Sina Atalay is with CERN, 1211 Meyrin, Switzerland, and also with the Boğaziçi University, Bebek/Istanbul 34342, Türkiye.

Mariusz Wozniak, Julien Dular, and Arjan Verweij are with CERN, 1211 Meyrin, Switzerland.

Nicolas Marsic and Sebastian Schöps are with the Technical University of Darmstadt, 64289 Darmstadt, Germany.

Christophe Geuzaine and Benoît Vanderheyden are with the University of Liège, 4000 Liège, Belgium.

Color versions of one or more figures in this article are available at <https://doi.org/10.1109/TASC.2023.3340648>.

Digital Object Identifier 10.1109/TASC.2023.3340648

thermal stability [2] resulting from a possibility for currents to bypass local normal zones [3], [4], [5]. Despite this, quenches are still possible in NI coils [6], [7], [8], [9], [10], [11]. To this end, quench detection and protection of NI coils require appropriate modeling and analysis methods.

Most commonly, simulations of NI coils are based on (distributed) network models; see [2] for a summary. For FE-based simulations, two-dimensional (2D) axisymmetric techniques based on a homogenization employing an anisotropic resistivity tensor have been proposed in 2020 [12]. More recently, in 2023, 2D axisymmetric models based on the Minimum Electro Magnetic Entropy Production (MEMEP) method have been studied [13].

However, NI coils commonly exhibit true three-dimensional (3D) geometries and quenches are intrinsically local effects. To comprehensively simulate quench, full 3D models are thus desirable. These are difficult due to the current flow across the turn-to-turn contact layer (T2TCL) [12], which has a high aspect ratio [14]. In [15], classical FE models with volumetric T2TCL have been used to study the AC loss of an NI pancake coil. They were, however, restricted to sinusoidal sources and lacking the thermal coupling. To ensure an accurate solution, the T2TCL requires a high number of degrees of freedom (DoF) in a classical FE method.

Recently, we proposed to collapse the T2TCL volumes to surfaces using a so-called thin shell approximation (TSA). First, a thermal TSA to represent thin insulation layers by considering the heat equation was introduced in [14]. Second, a magnetodynamic  $\vec{H} - \phi$  TSA was used to study the charge and discharge of NI coils in [16]. By replacing T2TCL volumes with surfaces, no volumetric mesh of the thin layer is required. This work proposes to combine the thermal TSA of [14] and the magnetodynamic TSA of [16] to model T2TCL with magneto-thermal T2TCL taking into account the coupling via *i*) non-linear material relations and *ii*) Joule losses.

One-dimensional (1D) Lagrange elements are used to discretize both temperature and magnetic field strength across the thickness of the T2TCL [17], [18]. As discussed in [19], the choice of formulation is important for robust and efficient simulations of systems with high-temperature superconductors (HTS). Since no ferromagnetic material exists in the computational domain, the  $\vec{H} - \phi$  formulation is preferred over  $\vec{A}$  formulations. Special care is needed to treat multiply connected domains, which is achieved using automatically created cohomology basis functions [20]. The HTS coated conductor (CC) is approximated by using a homogenization with anisotropic material properties which represent the multi-layered structure of the CC. In particular, the current sharing between the HTS and other layers is resolved.

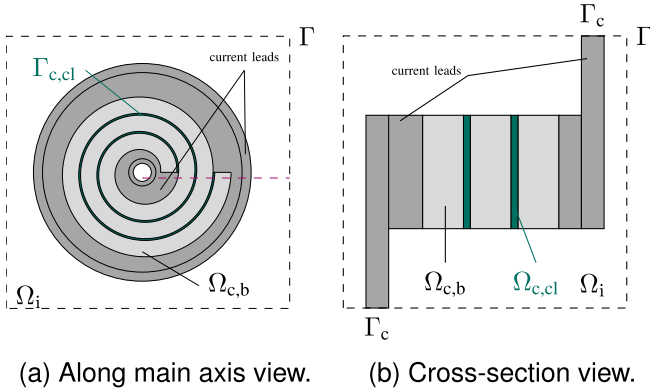


Fig. 1. Computational domain  $\Omega$  of the pancake coil with exterior boundary  $\partial\Omega = \Gamma$ . It consists of an insulating domain  $\Omega_i$  and a conducting domain  $\Omega_c$  which is divided into the bare CC  $\Omega_{c,b}$ , the T2TCL  $\Omega_{c,cl}$  and current leads. The cross-section view in (b) is taken at the purple dashed line shown in (a).

The magneto-thermal TSA is verified by comparison against a volumetric T2TCL model. The TSA is shown to be a robust alternative which produces accurate solutions with significantly reduced solution time and meshing effort. The source code with the details of the formulation is made available [21].

Section II presents the volumetric T2TCL model with the classical FE formulation. It is replaced with surface T2TCL with the coupled magneto-thermal TSA formulation in Section III with the derivation of the coupling terms. The model parameters of a powering cycle simulation of an NI coil with local defect and implementation details are summarized in Section IV. The results of these simulations are detailed in Section V. The major findings are summarized in Section VI.

## II. MAGNETO-THERMAL FORMULATION

The computational domain  $\Omega$  as depicted in Fig. 1 consists of a conducting domain  $\Omega_c$  and a non-conducting domain  $\Omega_i$ . The conducting domain consists of the bare homogenized CC  $\Omega_{c,b}$ , the T2TCL  $\Omega_{c,cl}$  as well as the current leads. It is bounded by  $\partial\Omega_c$  with outward normal vector  $\vec{n}_c$ . The boundary of the domain is denoted by  $\partial\Omega = \Gamma$  with outward normal vector  $\vec{n}$ . Furthermore,  $\Gamma_c$  denotes the terminals, i.e., the surfaces where the current leads coincide with  $\Gamma$ , which allow a current or a voltage source to be imposed.

The weak formulation of the coupled magnetodynamic [20] and thermal [22, Section 6.1.3.] problem is: From a solution at time  $t = 0$ , find  $\vec{H} \in H_{\phi,I}(\text{curl}, \Omega)$  and  $T \in H_g^1(\Omega_c)$  s.t.

$$\begin{aligned} & (\kappa \nabla T, \nabla T')_{\Omega_c} + (C_V \partial_t T, T')_{\Omega_c} \\ & = (\rho \vec{J} \cdot \vec{J}, T')_{\Omega_c} \quad \forall T' \in H_0^1(\Omega_c), \end{aligned} \quad (1)$$

$$\begin{aligned} & \left( \partial_t (\mu \vec{H}), \vec{H}' \right)_{\Omega} + (\rho \nabla \times \vec{H}, \nabla \times \vec{H}')_{\Omega_c} \\ & = 0 \quad \forall \vec{H}' \in H_{\phi,0}(\text{curl}, \Omega). \end{aligned} \quad (2)$$

Herein,  $\vec{H}$  is the magnetic field strength in  $\text{A m}^{-1}$ ,  $T$  the temperature in K,  $\kappa$  the thermal conductivity in  $\text{W m}^{-1} \text{K}^{-1}$ ,  $C_V$  the volumetric heat capacity in  $\text{J K}^{-1} \text{m}^{-3}$ ,  $\rho$  the electric resistivity in  $\Omega \text{m}$ ,  $\vec{J} = \nabla \times \vec{H}$  the electric current density in  $\text{A m}^{-2}$  and  $\mu$  the magnetic permeability in  $\text{H m}^{-1}$ . The volume integral in  $\Omega$  of the scalar product of the two arguments is denoted by  $(\cdot, \cdot)_{\Omega}$ .

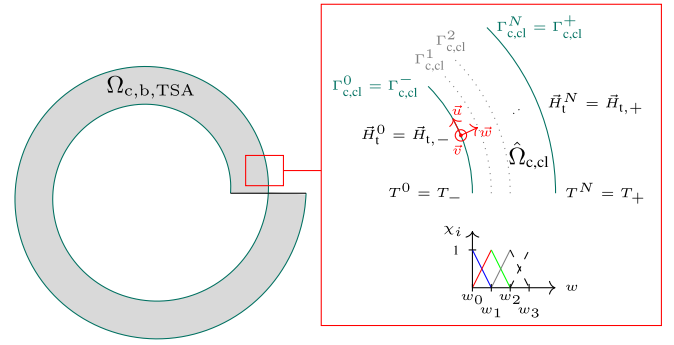


Fig. 2. One turn of the HTS pancake coil (top view): for the TSA approach, the T2TCL is represented by a virtual domain  $\hat{\Omega}_{c,cl}$  in which an internal FE discretization is used to solve the magneto-thermal problem.

The coupling between (1) and (2) appears in the Joule loss term, i.e., the right hand side of (1) as well as in the temperature and field dependencies of the materials.

We considered the boundary conditions

$$\vec{n} \times \vec{E} = 0 \quad \text{on } \Gamma \quad \stackrel{[23]}{\Rightarrow} \quad \vec{n} \cdot (\mu \vec{B}) = 0 \quad \text{on } \Gamma, \quad (3)$$

with the electric field  $\vec{E}$  in  $\text{V m}^{-1}$ , the magnetic flux density  $\vec{B} = \mu \vec{H}$  in T and

$$T = g \quad \text{on } \Gamma_c, \quad (4)$$

$$\vec{n}_c \cdot (\kappa \nabla T) = 0 \quad \text{on } \partial\Omega_c \setminus \Gamma_c, \quad (5)$$

imposing the temperature on the terminals and adiabatic conditions everywhere else. Furthermore,  $H_{\phi,I}(\text{curl}, \Omega)$  is the subspace of  $H(\text{curl}, \Omega)$  with vanishing curl in  $\Omega_i$  and strongly imposed source currents via cohomology basis functions [20]. Its subspace with zero current is  $H_{\phi,0}(\text{curl}, \Omega)$ . The subspace of  $H^1(\Omega_c)$  which fulfills the Dirichlet condition (4) is denoted as  $H_g^1(\Omega_c)$ . Its subspace with  $g = 0$  is  $H_0^1(\Omega_c)$ . To represent the layered structure of the CC, an anisotropic resistivity is used inside  $\Omega_{c,b}$ . A local coordinate system  $(\vec{u}, \vec{v}, \vec{w})$  is introduced as shown in Fig. 2 with  $\vec{u}$  in tangential direction along the spiral winding,  $\vec{v}$  in axial direction and  $\vec{w}$  normal to the spiral winding. In the local coordinate system, the resistivity reads

$$\rho_{uvw}|_{\Omega_{c,b}} = \text{diag}(\rho_{uu}, \rho_{vv}, \rho_{ww}). \quad (6)$$

In  $\vec{u}$ - and  $\vec{v}$ -direction, the layers of the CC are electrically connected in parallel with the equivalent resistance

$$\rho_{uu} = \rho_{vv} = \left( \frac{f_{\text{NC}}}{\rho_{\text{NC},uu}} + \frac{f_{\text{HTS}}}{\rho_{\text{HTS}}} \right)^{-1}, \quad (7)$$

with  $f_{\text{HTS}}$  the volume fraction of superconducting material in the CC,  $f_{\text{NC}} = 1 - f_{\text{HTS}}$  the fraction of non-superconducting materials (here, copper, silver, and Hastelloy) and  $\rho_{\text{NC},uu}$  the equivalent parallel resistivity of non-superconducting materials. The resistivity of the HTS is given by the power law, i.e.,

$$\rho_{\text{HTS}} = \frac{E_c}{J_c} \left( \frac{\|\vec{J}_{\text{HTS}}\|}{J_c} \right)^{n-1}, \quad (8)$$

with the critical electric field  $E_c = 1 \times 10^{-4} \text{ V m}^{-1}$  and the fit of the critical current density  $J_c(\|\vec{B}\|, T, \theta)$  from [24] with  $\theta$  the

TABLE I  
SUMMARY OF MODEL PARAMETERS

Description	Value
Power law $n$ -value	30
Critical current $I_c$	$I_c \left( \left\  \vec{B} \right\ , T, \theta \right)$ [24]
Critical current at $\vec{B} = 0$ and $T = 15$ K	780 A
ReBCO thickness	1.5 $\mu\text{m}$
{Cu, Hastelloy <sup>®</sup> , Ag} thickness	{42, 75, 1.5} $\mu\text{m}$ [24]
Source current $I_{\text{src}}$	Powering cycle (Fig. 5)
Number of turns $N_t$	24
Inner radius	5 mm*
Bare conductor width $w_t$	4 mm
T2TCL thickness $th_{\text{cl}}$	10 $\mu\text{m}$
T2TCL resistivity $\rho_{\text{cl}}$	$1.12 \times 10^{-4}$ $\Omega\text{m}$ [30]
T2TCL thermal conductivity $\kappa_{\text{cl}}$	Stainless steel [24]
T2TCL heat capacity $C_{V,\text{cl}}$	Stainless steel [24]
Initial temperature $T$ at $t = 0$ s	15 K
Local defect with $J_c = 0$	Turn 12.4 to 12.6 (Fig. 4)
Current lead material	Cu [24] with RRR = 100
Temperature boundary condition $g$	$g = 15$ K $\forall t$

\*This radius was chosen to aid visualization of the geometry and results.

angle between the tape wide surface and the  $\vec{B}$ -field. The current flowing in the HTS layer  $\vec{J}_{\text{HTS}}$  reads

$$\vec{J}_{\text{HTS}} = \frac{\lambda}{f_{\text{HTS}}} \left( \vec{J} \cdot \vec{u} \right) \vec{u} + \frac{\lambda}{f_{\text{HTS}}} \left( \vec{J} \cdot \vec{v} \right) \vec{v} + \left( \vec{J} \cdot \vec{w} \right) \vec{w}, \quad (9)$$

where the current sharing index  $\lambda$  is the fraction of current flowing in the HTS layer. A non-linear root-finding problem needs to be solved as detailed in [25, Section III.D] and [16] to find  $\lambda$ . All other parameters in (8) are presented in Table I.

In  $\vec{w}$ -direction, the equivalent series resistivity reads

$$\rho_{ww} = f_{\text{NC}} \rho_{\text{NC},ww} + f_{\text{HTS}} \rho_{\text{HTS}}, \quad (10)$$

with  $\rho_{\text{NC},ww}$  the equivalent resistivity of the series connection of the non-superconducting materials. In this work,  $J_c$  and consequently  $\rho_{\text{HTS}}$  are assumed to be the same in  $\vec{w}$  and  $\vec{u} - \vec{v}$  direction, but different functions could be used. The resistivity of the buffer layers can be accounted for in the contact resistivity.

The material tensor  $\rho_{uvw}$  needs to be represented in the Cartesian  $xyz$  coordinate system by using the transformation matrix from the local  $uvw$  to the Cartesian coordinates

$$M = [\vec{u}(x, y, z), \vec{v}(x, y, z), \vec{w}(x, y, z)], \quad (11)$$

with  $\vec{u}$ ,  $\vec{v}$  and  $\vec{w}$  understood as row vectors. In Cartesian coordinates, the resistivity tensor then reads

$$\rho|_{\Omega_{\text{c,b}}} = \rho_{xyz}|_{\Omega_{\text{c,b}}} = M \rho_{uvw}|_{\Omega_{\text{c,b}}} M^T. \quad (12)$$

The non-linear system is linearized using a quasi Newton-Raphson scheme where the derivatives of  $\rho_{\text{c,b}}$  w.r.t.  $\vec{J}$  is approximated using a finite difference scheme while all other derivatives are neglected.

The discretization of the magnetodynamics problem for pancake NI coils is discussed in detail in [16] while details for the thermal problem are found in [14]. The coupled problem is not discretized in a single monolithic linear system but two linear systems are created, one for (1) and one for (2), which are then solved sequentially inside the Newton-Raphson loop.

### III. THIN SHELL FORMULATION

In order to treat the T2TCL in a magneto-thermal setting, we propose to couple the TSA proposed in [14] and [16]. In order

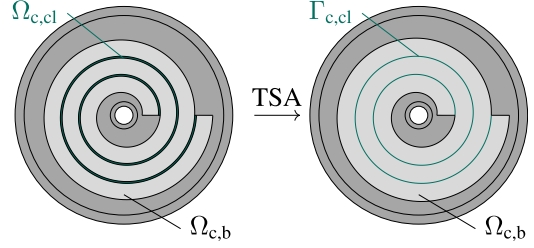


Fig. 3. HTS pancake coil (top view): for the TSA approach, the T2TCL volume  $\Omega_{\text{c,cl}}$  (left) is collapsed into the T2TCL surface  $\Gamma_{\text{c,cl}}$  (right).

to explain the coupling in detail afterwards, a summary of these previous papers is presented here. The main focus, however, is on the coupling of the two TSA.

First, the volumetric T2TCL  $\Omega_{\text{c,cl}}$  is replaced by a surface  $\Gamma_{\text{c,cl}}$  as shown in Fig. 3. As  $\Omega_{\text{c,cl}}$  is thermally and electrically conducting, the temperature and tangential magnetic field strength are discontinuous in order to represent temperature gradients and surface current densities. As proposed in [26], this discontinuity is introduced using dedicated basis functions for both  $T$  [14] and  $\vec{H}$  [16], rather than on the mesh level as proposed in [17]. Thanks to this choice, the thermal and magnetodynamic TSA can use the same mesh avoiding the need for interpolation between different meshes.

As shown in Fig. 2,  $T_+$  and  $T_-$  with support restricted to one of the two sides of  $\Gamma_{\text{c,cl}}$  are introduced as well as corresponding test functions  $T'_+$  and  $T'_-$ . The procedure is repeated with the magnetic field strength yielding  $\vec{H}_+$ ,  $\vec{H}_-$ ,  $\vec{H}'_+$ ,  $\vec{H}'_-$ . This approach leads to additional surface contributions in the weak formulations (1) and (2) [14], [16]. These contributions are used to consider an interface condition on  $\Gamma_{\text{c,cl}}$ .

This interface condition is built by an *internal FE discretization* of the weak formulations (1) and (2). This discretization takes place in the internal domain  $\hat{\Omega}_{\text{c,cl}}$  which is a representation of the T2TCL  $\Omega_{\text{c,cl}}$  (see Fig. 2). To build the internal FE discretization, a local coordinate system  $(\vec{u}, \vec{v}, \vec{w})$  is used with the same orientation as for the anisotropic material properties, i.e., with  $\vec{u}$  in tangential direction along the spiral,  $\vec{v}$  in axial direction and  $\vec{w}$  along the normal direction of  $\Gamma_{\text{c,cl}}$ . The domain  $\hat{\Omega}_{\text{c,cl}}$  is subdivided into  $N$  layers  $\hat{\Omega}_{\text{c,cl}}^{(k)}$  for  $k = 1, \dots, N$  with  $\hat{\Omega}_{\text{c,cl}} = \bigcup_{k=1}^N \hat{\Omega}_{\text{c,cl}}^{(k)}$  and  $\hat{\Omega}_{\text{c,cl}}^{(k)} := \Gamma_{\text{c,cl}}^{(k)} \times [w_{k-1}, w_k]$ . In each  $\hat{\Omega}_{\text{c,cl}}^{(k)}$ , we make a product ansatz

$$\vec{H}|_{\hat{\Omega}_{\text{c,cl}}^{(k)}}(u, v, w, t) = \sum_{j=k-1}^k \vec{H}_t^j(u, v, t) \chi_j(w), \quad (13)$$

$$T|_{\hat{\Omega}_{\text{c,cl}}^{(k)}}(u, v, w, t) = \sum_{j=k-1}^k T^j(u, v, t) \chi_j(w), \quad (14)$$

where  $\vec{H}_t^j$  is the tangential magnetic field strength on  $\Gamma_{\text{c,cl}}^{(j)}$  and  $\chi_j(w)$  the basis function along  $\vec{w}$ . The latter can be chosen to match the simulation needs (including higher order functions). In this work, we use first-order Lagrange basis functions

$$\chi_{k-1}(w) = \frac{w_k - w}{w_k - w_{k-1}} \quad \text{and} \quad \chi_k(w) = \frac{w - w_{k-1}}{w_k - w_{k-1}},$$

for both problems. Let us note that the functions do not have to be the same for the thermal and magnetodynamic problem.



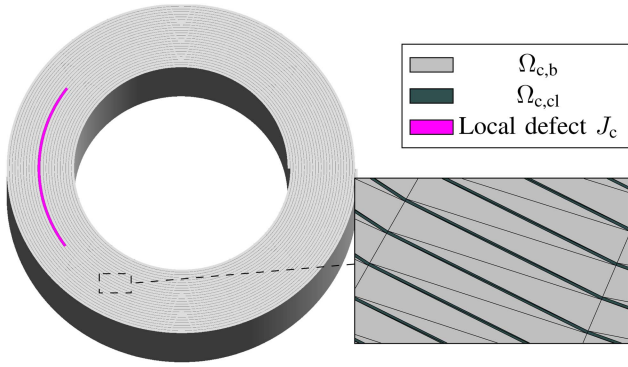


Fig. 4. Local defect and zoom on the mesh of the volumetric T2TCL.

However, by choosing them to be the same, one simplifies the implementation of the 1D FE integrals of the TSA formulation since it allows to reuse existing routines for their integration. The test functions  $T'$  and  $\vec{H}'$  are discretized with the same ansatz. This leads to a decomposition of the internal problem into surface integrals on  $\Gamma_{c,cl}^{(k)}$  and 1D FE integrals on  $[w_{k-1}, w_k]$ . The final expressions for the terms in weak formulation (1) and (2) are found in [14], [16], [18] except for the Joule losses term inside  $\hat{\Omega}_{c,cl}$ , that is,

$$\left(\rho \vec{J} \cdot \vec{J}, T'\right)_{\hat{\Omega}_{c,cl}} = \sum_{k=1}^N \left(\rho \vec{J} \cdot \vec{J}, T'\right)_{\hat{\Omega}_{c,cl}^{(k)}}. \quad (15)$$

Its derivation is detailed in Appendix A, which constitutes the first part of the coupling between magnetodynamics and heat equation. To appropriately account for the second part, i.e., the temperature- and field-dependence of the material parameters, the ansatzes (13) and (14) need to be used in the 1D FE integrals as derived in the appendix, alongside an appropriate numerical quadrature. In this work, Gaussian integration is used as it is readily available in the FE software. To account for the increased volume of  $\Omega_{c,b,TSA}$  compared to  $\Omega_{c,b}$ , a material scaling is introduced as detailed in Appendix B.

#### IV. IMPLEMENTATION AND SIMULATION SETUP

The magneto-thermal model, with and without the TSA, is implemented in the open-source framework GetDP 3.5 [27] using the Gmsh 4.11.0 [28] application programming interface to create the geometry and mesh. It also creates the cohomology basis functions required for the  $\vec{H} - \phi$  formulation [20]. Lowest order basis functions are used and as the T2TCL consists of only one material, the TSA is used with  $N = 1$ . An adaptive implicit Euler scheme is used for time integration [29].

All important parameters regarding the coil geometry and simulation setup are given in Table I. A local defect with  $J_c = 0$  is introduced to highlight the current diversion across the T2TCL, a mechanism that increases the thermal stability of NI coils. The local defect is depicted in Fig. 4 which also shows the mesh of the geometry with volumetric T2TCL.

#### V. POWERING CYCLE SIMULATION WITH LOCAL DEFECT

For verification, the powering cycle of the NI coil is simulated using three models; *i) vol*: a fine-meshed model with volumetric T2TCL, *ii) TSAf*: a T2TCL TSA model which uses the same mesh structure inside  $\Omega_{c,b}$  as the *vol* model and *iii) TSAc*: a

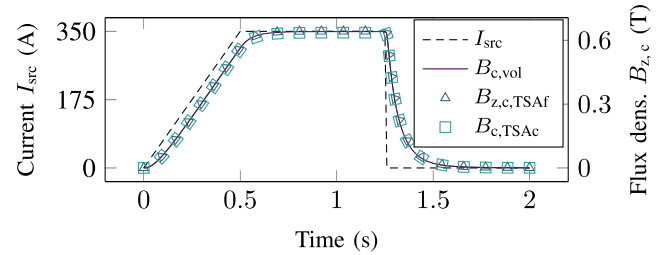


Fig. 5. Source current  $I_{src}$  and the central axial magn. flux density  $B_{z,c}$ .

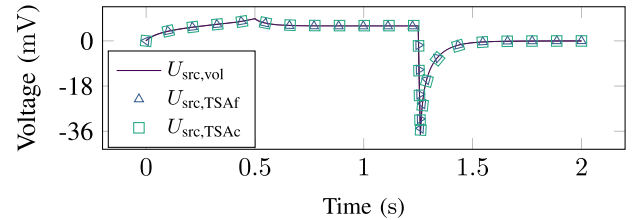


Fig. 6. Coil terminals voltages  $U_{src}$  for all models.

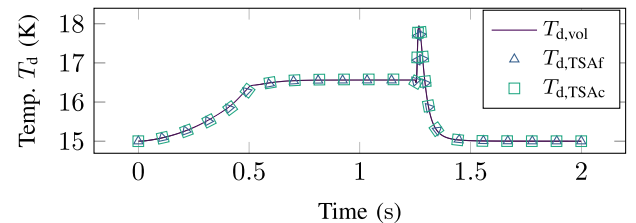
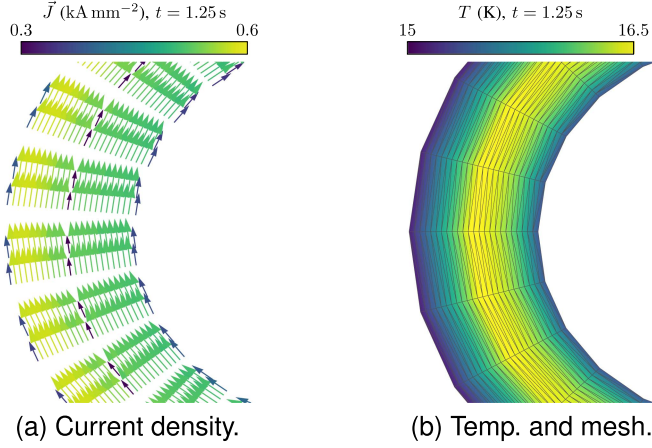


Fig. 7. Temperature at the center of the local defect for all models.

coarse-meshed T2TCL model (see Fig. 8(a) for the TSAc mesh). It has been proven difficult to use coarsely meshed models with volumetric T2TCL, either because of failure to automatically create suitable meshes or convergence issues due to the high aspect ratio of mesh elements. The TSA T2TCL models have been more robust and the aforementioned problems did not occur. Thus, it is possible to use coarse mesh with the TSA while achieving an accurate solution.

The applied source current and axial central magnetic flux density are depicted in Fig. 5 for all three models. The magnetic field is delayed w.r.t. the source current due to the radial currents and decays exponentially after the sudden discharge. All three models are in good agreement. The same is true for voltage between the coil terminals which is shown in Fig. 6. During charging and discharging, the absolute value of the voltage is highest as the radial currents flow in the highly resistive T2TCL. It does not decay to zero during the current plateau as *i)* the current leads are made of copper and *ii)* radial currents are crossing the T2TCL to divert around the local defect. The current diversion is depicted in Fig. 8(a) and the local temperature hot spot at the defect position in Fig. 8(b). Thanks to the current diversion and the cooling applied at the coil terminals using boundary condition (4), the local defect does not cause a thermal runaway as seen in Fig. 7. During charging, the temperature increases due to the currents across the T2TCL. During the current plateau, the heat generated by the currents across the T2TCL is removed by the cooling yielding a constant temperature. During the fast discharge, the large T2TCL currents first

Fig. 8. Current by-pass and temperature distribution at  $t = 1.25$  s.TABLE II  
NUMBER OF DOF AND TOTAL SOLUTION TIME OF THE THREE MODELS

Description	vol	TSAf	TSAc
Number of DoF thermal system	14907	14896	5229
Number of DoF magnetodynamic system	49740	39678	13090
Total solution time in h	17.4	16.9	5.05

cause a significant temperature increase which is then cooled down subsequently.

Having shown the accuracy of the TSA approach, the number of DoF and solution time are shown in Table II. Let us note that the implementation of the finite difference derivative makes heavy use of GetDP's scripting language. While this is convenient for the implementation, this increases significantly the time required for assembly of the linear systems and thus also the total solution time required. It does not have an influence on the relative comparison of solution times between the models but only on the absolute timing. The TSAc model has 71% fewer DoF and is 3.4 times faster than the vol model. For vanishing T2TCL thickness (i.e., directly touching turns), it becomes increasingly difficult to use a volumetric T2TCL [14]. The TSA then is the only practical method that is expected to lead to an accurate solution. Its efficiency allows resolving each turn in the mesh. This enables local quench simulation on the level of individual turns (or parts of them).

## VI. CONCLUSION

A coupled magneto-thermal TSA has been presented to model the T2TCL in the FE analysis of HTS NI coils in 3D. The formulation has been implemented in the open-source FE framework Gmsh/GetDP and a reference implementation has been made publicly available. The numerical results of a powering cycle of a model NI coil have been verified against a model with volumetric T2TCL showing excellent agreement. The TSA leads to a significantly reduced number of DoF, solution time and simplifies the creation of high-quality meshes. Its robustness and efficiency enable automated models resolving each turn to capture local effects like quench.

## APPENDIX A

### DERIVATION OF JOULE LOSS EXPRESSION

From the representation of  $\vec{H}$  in  $\hat{\Omega}_{c,cl}^{(k)}$  in (13), we find that

$$\vec{J}|_{\hat{\Omega}_{c,cl}^{(k)}} = \nabla \times \vec{H}|_{\hat{\Omega}_{c,cl}^{(k)}} = \nabla \times \left[ \sum_{j=k-1}^k \vec{H}_t^j \chi_j \right], \quad (16)$$

$$= \sum_{j=k-1}^k \nabla \chi_j \times \vec{H}_t^j + \chi_j \nabla \times \vec{H}_t^j, \quad (17)$$

$$= \vec{w} \times \frac{\vec{H}_t^k - \vec{H}_t^{k-1}}{w_k - w_{k-1}} + \sum_{j=k-1}^k \chi_j \nabla \times \vec{H}_t^j. \quad (18)$$

Note that first summand is orthogonal to the  $\vec{w}$ -direction while the second is in  $\vec{w}$ -direction. Using (18), the ansatz (14) for  $T'$  and  $l \in \{k-1, k\}$ , the Joule losses in the TSA evaluate to

$$\begin{aligned} & \left( \rho \vec{J} \cdot \vec{J}, T' \right)_{\hat{\Omega}_{c,cl}^{(k)}} \\ &= \left( \rho \left\| \frac{\vec{H}_t^k - \vec{H}_t^{k-1}}{w_k - w_{k-1}} \right\|^2, T_l' \chi_l \right)_{\hat{\Omega}_{c,cl}^{(k)}} \\ &+ \left( \rho \sum_{i=k-1}^k \left( \chi_i \nabla \times \vec{H}_t^i \right) \cdot \sum_{j=k-1}^k \left( \chi_j \nabla \times \vec{H}_t^j \right), T_l' \chi_l \right)_{\hat{\Omega}_{c,cl}^{(k)}} \\ &= \left\langle f_l \left\| \frac{\vec{H}_t^k - \vec{H}_t^{k-1}}{w_k - w_{k-1}} \right\|^2, T_l' \right\rangle_{\Gamma_{c,cl}^{(k)}} \\ &+ \sum_{i=k-1}^k \sum_{j=k-1}^k \left\langle c_{ijl} \nabla \times \vec{H}_t^i \cdot \nabla \times \vec{H}_t^j, T_l' \right\rangle_{\Gamma_{c,cl}^{(k)}}. \end{aligned}$$

Herein,  $\langle \cdot, \cdot \rangle_{\Gamma}$  denotes the surface integral of the scalar product of its two arguments on  $\Gamma$ . We introduced the 1D FE integrals

$$f_l = \int_{w_{k-1}}^{w_k} \rho \chi_l dw \quad \text{and} \quad c_{ijl} = \int_{w_{k-1}}^{w_k} \rho \chi_i \chi_j \chi_l dw.$$

This concludes the decomposition into surface integrals on  $\Gamma_{c,cl}^{(k)}$  and 1D FE integrals in  $[w_{k-1}, w_k]$ , alleviating the need for a volumetric mesh representation of  $\Omega_{c,cl}$ .

## APPENDIX B

### MATERIAL SCALING FOR TSA MODEL

Using the scaling factor

$$p = \frac{|\Omega_{c,cl}| + |\Omega_{c,b}|}{|\Omega_{c,b}|} = 1 + \frac{|\Omega_{c,cl}|}{|\Omega_{c,b}|} = \frac{|\Omega_{c,b,TSA}|}{|\Omega_{c,b}|}, \quad (19)$$

the material parameters of  $\Omega_{c,b,TSA}$  are scaled by

$$\begin{aligned} \kappa_{uu}|_{\Omega_{c,b,TSA}} &= p^{-1} \kappa_{uu}|_{\Omega_{c,b}}, & \kappa_{ww}|_{\Omega_{c,b,TSA}} &= p \kappa_{ww}|_{\Omega_{c,b}}, \\ \rho_{uu}|_{\Omega_{c,b,TSA}} &= p \rho_{uu}|_{\Omega_{c,b}}, & \rho_{ww}|_{\Omega_{c,b,TSA}} &= p^{-1} \rho_{ww}|_{\Omega_{c,b}}, \\ C_V|_{\Omega_{c,b,TSA}} &= p^{-1} C_V|_{\Omega_{c,b}}, & J_c|_{\Omega_{c,b,TSA}} &= p^{-1} J_c|_{\Omega_{c,b}}. \end{aligned}$$

## REFERENCES

- [1] S. Hahn, D. K. Park, J. Bascunan, and Y. Iwasa, "HTS pancake coils without turn-to-turn insulation," *IEEE Trans. Appl. Supercond.*, vol. 21, no. 3, pp. 1592–1595, Jun. 2011, doi: [10.1109/TASC.2010.2093492](https://doi.org/10.1109/TASC.2010.2093492).
- [2] S. Hahn, K. Kim, K. Kim, and Y. Iwasa, "Current status of and challenges for no-insulation HTS winding technique," *TEION KOGAKU (J. Cryogenics Supercond. Soc. Jpn.)*, vol. 53, pp. 2–9, 2018, doi: [10.2221/jcsj.53.2](https://doi.org/10.2221/jcsj.53.2).
- [3] T. Wang et al., "Analyses of transient behaviors of no-insulation REBCO pancake coils during sudden discharging and overcurrent," *IEEE Trans. Appl. Supercond.*, vol. 25, no. 3, 2015, Art. no. 4603409, doi: [10.1109/TASC.2015.2393058](https://doi.org/10.1109/TASC.2015.2393058).
- [4] Y. Wang, W. K. Chan, and J. Schwartz, "Self-protection mechanisms in no-insulation (RE)Ba<sub>2</sub>Cu<sub>3</sub>O<sub>x</sub> high temperature superconductor pancake coils," *Supercond. Sci. Technol.*, vol. 29, no. 4, 2016, Art. no. 045007, doi: [10.1088/0953-2048/29/4/045007](https://doi.org/10.1088/0953-2048/29/4/045007).
- [5] S. Hahn et al., "Defect-irrelevant" behavior of a no-insulation pancake coil wound with REBCO tapes containing multiple defects," *Supercond. Sci. Technol.*, vol. 29, no. 10, Sep. 2016, Art. no. 105017, doi: [10.1088/0953-2048/29/10/105017](https://doi.org/10.1088/0953-2048/29/10/105017).
- [6] K. Kim et al., "Quench behavior of a no-insulation coil wound with stainless steel cladding REBCO tape at 4.2 k," *Supercond. Sci. Technol.*, vol. 30, no. 7, May 2017, Art. no. 075001, doi: [10.1088/1361-6668/aa6a8b](https://doi.org/10.1088/1361-6668/aa6a8b).
- [7] Y. Yanagisawa et al., "Basic mechanism of self-healing from thermal runaway for uninsulated REBCO pancake coils," *Physica C: Supercond.*, vol. 499, pp. 40–44, 2014, doi: [10.1016/j.physc.2014.02.002](https://doi.org/10.1016/j.physc.2014.02.002).
- [8] S. Hahn et al., "45.5-Tesla direct-current magnetic field generated with a high-temperature superconducting magnet," *Nature*, vol. 570, pp. 496–499, 2019, doi: [10.1038/s41586-019-1293-1](https://doi.org/10.1038/s41586-019-1293-1).
- [9] P. C. Michael et al., "Assembly and test of a 3-nested-coil 800-MHz REBCO insert (H800) for the MIT 1.3 GHz LTS/HTS NMR magnet," *IEEE Trans. Appl. Supercond.*, vol. 29, no. 5, Aug. 2019, Art. no. 4300706, doi: [10.1109/TASC.2019.2901246](https://doi.org/10.1109/TASC.2019.2901246).
- [10] Y. Suetomi et al., "Quench and self-protecting behaviour of an intra-layer no-insulation (LNI) REBCO coil at 31.4 T," *Supercond. Sci. Technol.*, vol. 34, no. 6, 2021, Art. no. 064003, doi: [10.1088/1361-6668/abf54e](https://doi.org/10.1088/1361-6668/abf54e).
- [11] L. Shao et al., "Degradation characteristics of a 20 T REBCO insert magnet after a 4.2 K standalone test," *IEEE Trans. Appl. Supercond.*, vol. 33, no. 5, Aug. 2023, Art. no. 4300306, doi: [10.1109/TASC.2023.3254483](https://doi.org/10.1109/TASC.2023.3254483).
- [12] R. C. Mataira, M. D. Ainslie, R. A. Badcock, and C. W. Bumby, "Finite-element modelling of no-insulation HTS coils using rotated anisotropic resistivity," *Supercond. Sci. Technol.*, vol. 33, no. 8, Jun. 2020, Art. no. 08LT01, doi: [10.1088/1361-6668/ab9688](https://doi.org/10.1088/1361-6668/ab9688).
- [13] E. Pardo and P. Fazilleau, "Fast and accurate electromagnetic modeling of non-insulated and metal-insulated REBCO magnets," 2023, doi: [10.48550/arXiv.2309.02249](https://doi.org/10.48550/arXiv.2309.02249), *arXiv:2309.02249*.
- [14] E. Schnaubelt, M. Wozniak, and S. Schöps, "Thermal thin shell approximation towards finite element quench simulation," *Supercond. Sci. Technol.*, vol. 36, no. 4, 2023, Art. no. 044004, doi: [10.1088/1361-6668/acbeea](https://doi.org/10.1088/1361-6668/acbeea).
- [15] X. Wang et al., "Magnetization loss of no-insulation coil for an electrodynamic suspension system," *Supercond. Sci. Technol.*, vol. 34, no. 6, 2021, Art. no. 065007, doi: [10.1088/1361-6668/abe18c](https://doi.org/10.1088/1361-6668/abe18c).
- [16] E. Schnaubelt, M. Wozniak, S. Schöps, and A. Verweij, "Electromagnetic simulation of no-insulation coils using H- $\phi$  thin shell approximation," *IEEE Trans. Appl. Supercond.*, vol. 33, no. 5, Aug. 2023, Art. no. 4900906, doi: [10.1109/TASC.2023.3258905](https://doi.org/10.1109/TASC.2023.3258905).
- [17] B. de Sousa Alves, V. Lahtinen, M. Laforest, and F. Sirois, "Thin-shell approach for modeling superconducting tapes in the H- $\phi$  finite-element formulation," *Supercond. Sci. Technol.*, vol. 35, no. 2, Dec. 2021, Art. no. 024001, doi: [10.1088/1361-6668/ac3f9e](https://doi.org/10.1088/1361-6668/ac3f9e).
- [18] B. de Sousa Alves, M. Laforest, and F. Sirois, "3-D finite-element thin-shell model for high-temperature superconducting tapes," *IEEE Trans. Appl. Supercond.*, vol. 32, no. 3, Apr. 2022, Art. no. 7500411, doi: [10.1109/TASC.2022.3143076](https://doi.org/10.1109/TASC.2022.3143076).
- [19] J. Dular, C. Geuzaine, and B. Vanderheyden, "Finite-element formulations for systems with high-temperature superconductors," *IEEE Trans. Appl. Supercond.*, vol. 30, no. 3, Apr. 2020, Art. no. 8200113, doi: [10.1109/TASC.2019.2935429](https://doi.org/10.1109/TASC.2019.2935429).
- [20] M. S. Pelliikka, L. Suuriniemi Kettunen, and C. Geuzaine, "Homology and cohomology computation in finite element modeling," *SIAM J. Sci. Comput.*, vol. 35, no. 5, pp. B1195–B1214, 2013, doi: [10.1137/130906556](https://doi.org/10.1137/130906556).
- [21] E. Schnaubelt, S. Atalay, and J. Dular, "Magneto-thermal thin shell approximation for FE analysis of no-insulation coils," *Zenodo*, Nov. 2023, doi: [10.5281/zenodo.8353188](https://doi.org/10.5281/zenodo.8353188). [Online]. Available: <https://zenodo.org/record/8353188>
- [22] A. Ern and J.-L. Guermond, *Theory and Practice of Finite Elements*. New York, NY, USA: Springer, ISBN 978-0-387-20574-8, 2004, doi: [10.1007/978-1-4757-4355-5](https://doi.org/10.1007/978-1-4757-4355-5).
- [23] P. Dular, P. Kuo-Peng, C. Geuzaine, N. Sadowski, and J. P. A. Bastos, "Dual magnetodynamic formulations and their source fields associated with massive and stranded inductors," *IEEE Trans. Magn.*, vol. 36, no. 4, pp. 1293–1299, Jul. 2000, doi: [10.1109/20.877677](https://doi.org/10.1109/20.877677).
- [24] "STEAM Materials Library GitLab Repository," 2023. [Online]. Available: <https://gitlab.cern.ch/steam/steam-material-library>
- [25] L. Bortot et al., "A coupled A-H formulation for magneto-thermal transients in high-temperature superconducting magnets," *IEEE Trans. Appl. Supercond.*, vol. 30, no. 5, Aug. 2020, Art. no. 4900911, doi: [10.1109/TASC.2020.2969476](https://doi.org/10.1109/TASC.2020.2969476).
- [26] C. Geuzaine, P. Dular, and W. Legros, "Dual formulations for the modeling of thin electromagnetic shells using edge elements," *IEEE Trans. Magn.*, vol. 36, no. 4, pp. 799–803, Jul. 2000, doi: [10.1109/20.877566](https://doi.org/10.1109/20.877566).
- [27] P. Dular, C. Geuzaine, F. Henrotte, and W. Legros, "A general environment for the treatment of discrete problems and its application to the finite element method," *IEEE Trans. Magn.*, vol. 34, no. 5, pp. 3395–3398, Sep. 1998, doi: [10.1109/20.717799](https://doi.org/10.1109/20.717799).
- [28] C. Geuzaine and J.-F. Remacle, "Gmsh: A 3-D finite element mesh generator with built-in pre- and post-processing facilities," *Int. J. Numer. Methods Eng.*, vol. 79, pp. 1309–1331, 2009, doi: [10.1002/nme.2579](https://doi.org/10.1002/nme.2579).
- [29] U. M. Ascher and L. R. Petzold, *Computer Methods for Ordinary Differential Equations and Differential-Algebraic Equations*. Philadelphia, PA, USA: SIAM, ISBN: 978-0898714128, 1998.
- [30] J. Lee, J. Mun, J. Kim, and S. Kim, "Investigation on the electrical contact resistance of soldered metal insulation REBCO coil," *IEEE Trans. Appl. Supercond.*, vol. 31, no. 5, Aug. 2021, Art. no. 4601205, doi: [10.1109/TASC.2021.3063653](https://doi.org/10.1109/TASC.2021.3063653).